Metrology for spatial interferometry V

Yekta Gürsel

Jet Propulsion Laboratory
California Institute of Technology
4800 Oak Grove Dr., Pasadena, CA 91109

ABSTRACT

The proposed Space Interferometry Mission (SIM) spacecraft designs include high resolution stellar interferometers for micro-arc-second accuracy astrometric measurements. These stellar interferometers require picometer accuracy one dimensional metrology gauges, surface metrology gauges and 3-dimensional metrology gauges to measure the required distances or to calibrate the fiducials that define the end points of the interferometric paths. The absolute metrology gauges required by these interferometers can be considerably less accurate due to the careful design of the astrometric interferometers and the fiducials on the spacecraft.

An auto-aligning, 3-dimensional metrology gauge constructed using the sub-picometer linear metrology gauges was described in earlier papers. The sub-nanometer, in-vacuum tracking results from this 3-dimensional metrology gauge are presented. The resulting jitter is analyzed and is shown to be caused by thermal drift in the alignment of the gauge heads, warpage of the base table and the time-dependent tilt of the experiment as a whole.

The aberrations in the light beams of the laser distance gauges can result in errors in the distance measurements performed using these gauges. Simulations using spot shapes and aberrations present in a realistic measurement system used in a stellar interferometer in space are performed to quantify the amount of expected errors. The results of these simulations are presented.

Open-faced, hollow corner cube retroreflectors are traditionally used as fiducials in the one-dimensional relative and absolute metrology gauges and the 3-dimensional metrology gauge. These are narrow field of view fiducials that can not accomodate interferometers that need access over much wider fields of view. Attempts had been made to increase the field of view of these fiducials by putting several of them together on the same block of glass[6] [7]. These designs have not achieved a common corner co-location of better than 1 μm due to purely technical, but hard to overcome difficulties.

A solid glass, one piece, 4π steradian field of view and easy to manufacture fiducial design is presented that allows common corner co-location within few tens of nanometers. The spatial and temporal stability of the common corner is achieved by carefully controlling the fiducial temperature drift and jitter to less than 1 millidegree Celcius.

1. INTRODUCTION

Very high resolution spatial interferometry requires picometer level one-dimensional metrology, surface metrology and 3-dimensional metrology. The absolute distance measurements with accuracies of only 1 part in a million are required due to the careful design of fiducials in spacecraft designs like the proposed Space Interferometry Mission (SIM) and others[9] [6] [10] [11], carrying high resolution stellar interferometers.

In five previous papers[1] [2] [3] [4] [5]a relative metrology gauge capable of sub-picometer accuracy, a surface metrology gauge with sub-nanometer repeatability, and a completely functional absolute metrology gauge with a repeatability of nearly of 1 part in 10^6, and in-air test results from a 3-dimensional metrology gauge were described.

In what follows, I will describe the first in-vacuum results from the 3-dimensional metrology gauge. The residual jitter obtained in vacuum is analyzed and it is shown to be caused by thermal drift in the alignment of the gauge heads, warpage of the base table and the time-dependent tilt of the experiment as a whole. The resonances of the experimental system contribute a little to the residual jitter.

Next, raster scans of the surface of an open faced, hollow corner-cube retroreflector near its corner are presented.

The repeatability of the raster scans are directly related to the residual jitter present in the 3-dimensional metrology gauge.

A direct test of the structural noise follows the raster scans of the measurement corner cube surface. An analysis linking the noise detected to the tracking jitter and to the surface raster scan repatability is presented.

A list of implemented improvements to the 3-dimensional gauge system is discussed. The result of these improvements will be presented in the subsequent paper.

The aberrations in the light beams of the laser distance gauges can result in errors in the distance measurements performed using these gauges. Simulations, using spot shapes and aberrations present in a realistic measurement system used in a stellar interferometer in space are performed to quantify the amount of expected errors. The results of these simulations are presented.

Finally, a wide angle fiducial design that overcomes some of the difficulties inherent in the open faced, hollow, corner-cube retroreflectors and their multi-part derivatives is presented. The design uses an existing glass type and existing polishing techniques to achieve common corner co-location within few tens of nanometers in a one piece, solid glass fiducial. The temporal stability of the common corner is achieved by carefully controlling the temperature drift and the temperature jitter of the fiducial to less than 1 millidegree Celcius[3][8].

2. 3-D METROLOGY GAUGE

2.1. 3-dimensional Tracking in Vacuum

The tracking performance is characterized by the residual jitter left behind after the constant base plate surveying is solved for[5]. The in-air jitter value of the 3-dimensional metrology gauge was 600 pm rms for motions of the measurement corner cube of the order of 10 wavelengths of OPD at a wavelength of 1319 nm.

When the vacuum chamber containing the 3-dimensional metrology gauge was evacuated, many phenomena that were absent in the in-air experiment surfaced. These were the initial warping of the invar base plate due to the trapped air inside and the creaking of the invar plate. The warpage of the base plate resulted in a misaligned experiment. This was corrected by moving the measurement corner cube to a new position using the coarse motion stages, and re-pointing the metrology heads using the dithering piezo-electric actuators. The creaking of the table was observed as sudden, large amplitude (60 nm or larger) changes in the recorded position of the measurement corner cube. Eventually (after a month in vacuum) all creaking stopped and the base table assumed a new shape that changed little as the chamber cycled between the atmospheric pressure and 10 milliTorr level vacuum. The immediate advantage of vacuum was observed as the immensely improved temperature stability: The experiment temperature changed only a few millidegrees of Celcius for a duration of several hours.

The 3-dimensional metrology gauge is operated in the non-dithered mode in vacuum on seismic isolation tracking the measurement corner cube for an approximate total motion of 25 microns, moving away from the plane of the heads. When the motion of the measurement corner cube is solved for each tetrahedra using the formulas and the crude survey given in the previous paper[5], the solutions for different tetrahedra differ by an amount linearly proportional to the motion of the measurement corner cube. This amount is about 8 to 10 nm per wavelength of OPD motion, matching in the in-air figures. Since the surveying is crude, a fit is performed using all available data to determine the final positions of the heads as well as the motion of the measurement corner cube by minimizing the difference in the motion reported by all eight tetrahedra.

Figs. 1, 2, 3 show the detected motion of the measurement corner cube by tetrahedron #1 in x, y and z coordinates.

Figs. 4, 5, 6 show the difference between what is measured by tetrahedron #1 and all the other tetrahedra in x, y and z coordinates respectively in vacuum. The tetrahedra are distinguished by different line styles in the plots.

A comparison of these figures with those given in the previous paper[5] immediately reveals that the root-mean-squared jitter observed in vacuum is virtually the same as the rms jitter observed in air: 600 pm rms. It is clear that the detected jitter that should have been about few tens of picometers rms in vacuum is not produced by

Figure 1: The x coordinate of the motion detected by tetrahedron #1 in vacuum
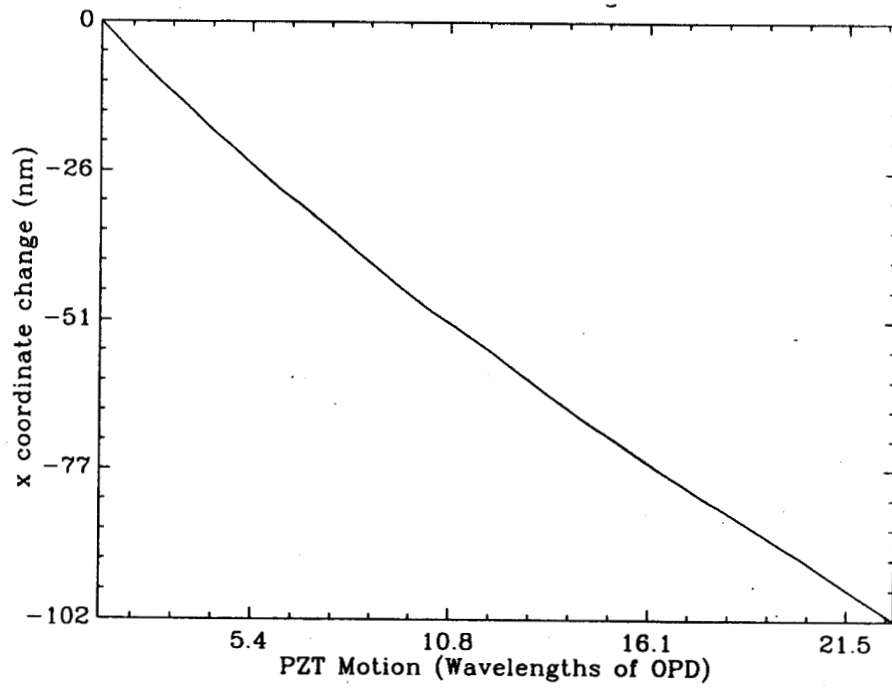

Figure 2: The y coordinate of the motion detected by tetrahedron #1 in vacuum
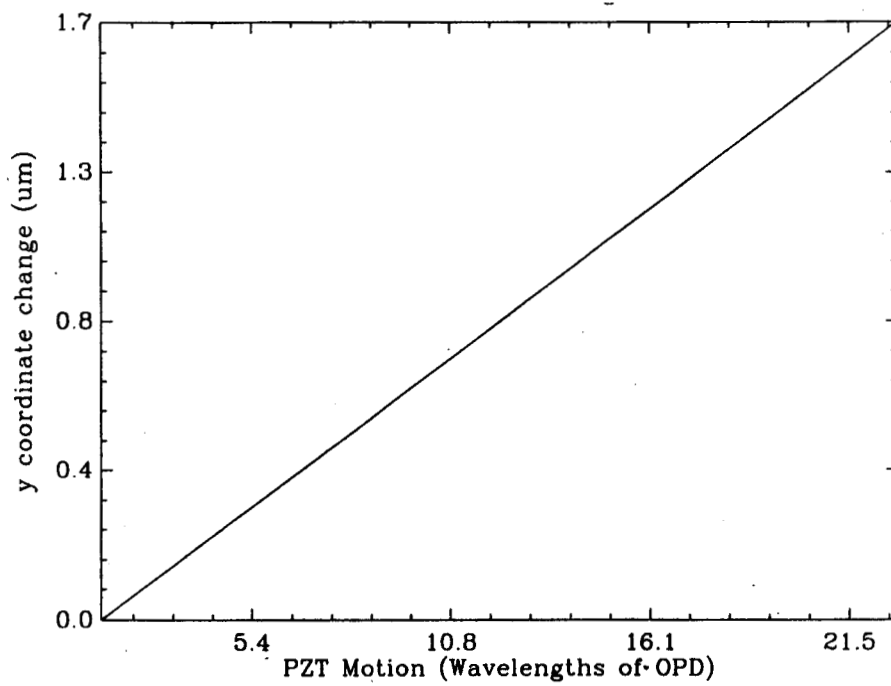
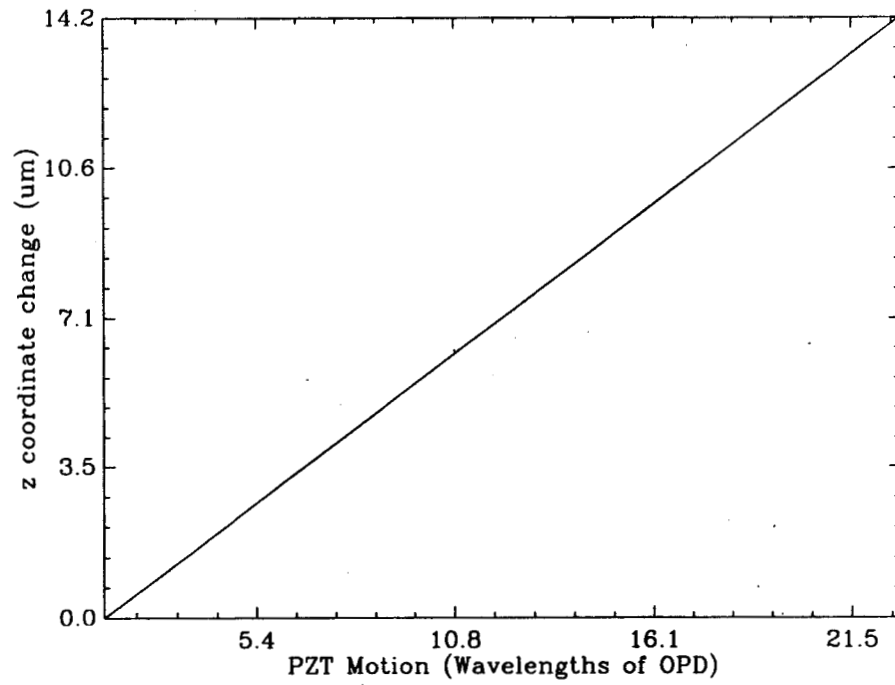Figure 3: The z coordinate of the motion detected by tetrahedron #1 in vacuum

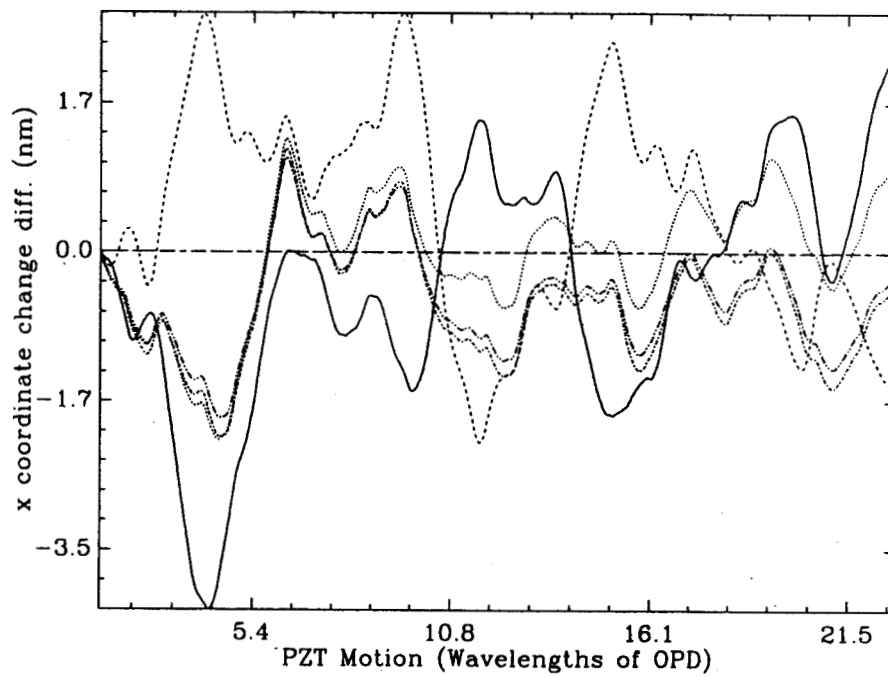Figure 4: The x coordinate difference between tetrahedron #1 and all others in vacuum

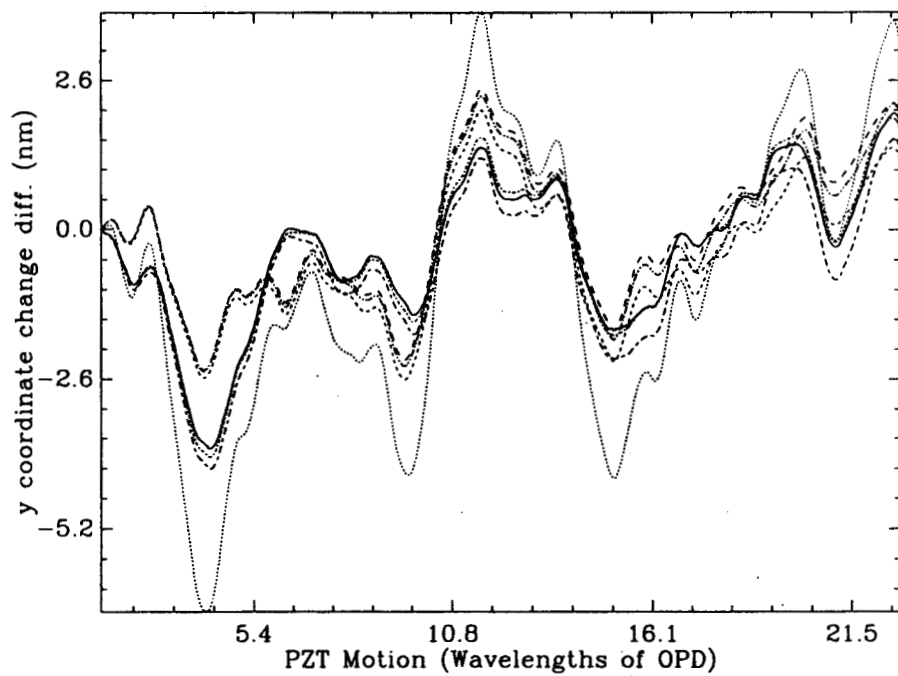Figure 5: The y coordinate difference between tetrahedron #1 and all others in vacuum
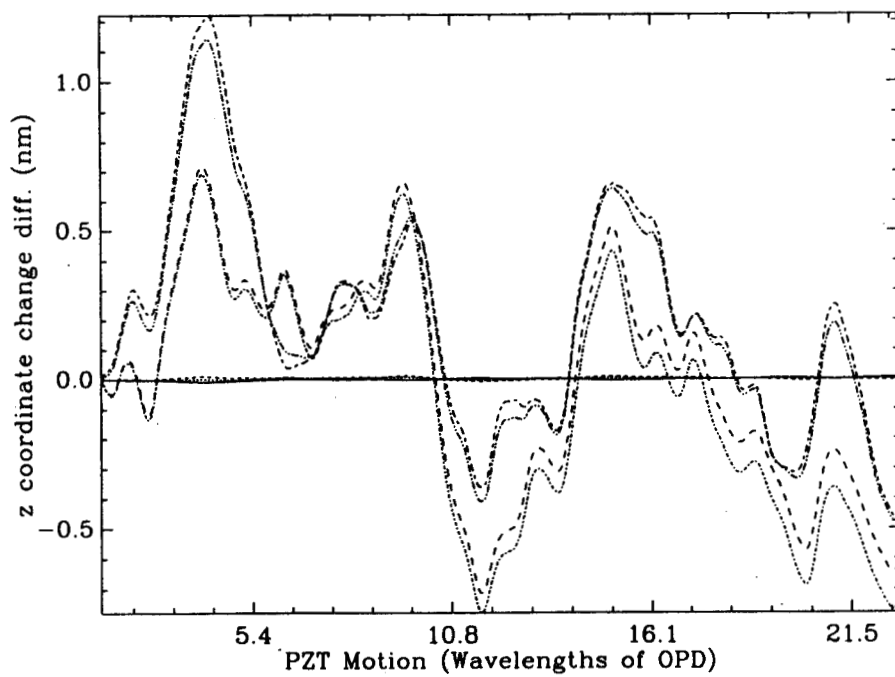

Figure 6: The z coordinate difference between tetrahedron #1 and all others in vacuum

air turbulence. This does not mean, however, that the ultimate jitter value could be obtained by keeping the experiment at atmospheric pressure. The vacuum environment is a lot more stable than the experimental environment at atmospheric pressure. Possible sources for the observed jitter are the thermal drifts of the experimental configuration, pressure change induced problems, the structural noise (sub-nanometer creaks), and of course, the measurement corner cube and the head reference corner cubes themselves.

2.2. Raster Scans of the Measurement Corner Cube

The surface irregularities of the measurement corner cube can contribute to the residual jitter in the 3-dimensional metrology tracking experiments, especially if the heads are drifting in alignment. In order to quantify these surface irregularities and also to show that the virtual corner of the measurement corner cube can be defined without any ambiguity, raster scans of the corner area of the measurement corner cube were performed, using one of the metrology heads.

In the 3-dimensional metrology apparatus, a reference corner cube that is a part of a metrology head does not move with the scanning metrology head. When raster scans are performed by tilting the metrology heads in two orthogonal axes, the laser beam of the gauge moves on the surfaces of both the reference and the measurement corner cubes. However, a reference corner cube is located much closer to the point of rotation of the laser beam than the measurement corner cube. The ratio of the "lever arms" is about 1:20.

The raster scans are performed by tilting a head through two orthogonal axes using three piezo-electric actuators attached to the base of the head. The laser beam performs a square, 10 by 10 raster scan of the corner cube surface collecting data for 2 seconds at each step and spending 1 second to move smoothly between the steps. The total range of the scan is 540 micro-radians in each axis, corresponding to x and y excursions of 0.46 mm on the surface of the measurement corner cube.

The initial scans were badly affected by malfunctioning 8-bit DAC's that drove the tilt actuators. In addition, the sharp DAC steps caused the fast responding actuators to ring. This ringing, the drifts in electronics and line frequency leakage also contributed adversely to the repeatability of the measurement corner cube raster scans. After all of the technical problems mentioned above were fixed, the 3-dimensional metrology gauge started producing sub-nanometer repeatability raster scans.

Fig. 7 shows the properly calibrated result of a typical 10 by 10 scan. The scanning geometry as well as the raster scan order are also illustrated. The "ribbed" structure superimposed on the gently curving "terrain" is unlikely to be a feature on the surface of the corner cube. It is a highly repeatable systematic effect that follows the raster scan order. This is traced to the DAC's driving the piezo-electric actuators.

Fig. 8 shows the difference between two subsequent raster scans. The residual is free of any significant systematic features.

Fig. 9 shows the difference between the first surface scan in a set and the subsequent scans in the same set. As time passes, the drifts in the head central position causes the long-term, random walk type drift shown.

Fig. 10 shows the difference between subsequent surface scans in the same set as in Fig. 9. The difference curve is without any appreciable drift and its root-mean-squared jitter is about 264 pm rms for about 10 subsequent raster scans. This value matches the residual jitter very well in the tracked z motion of the measurement corner cube (see Fig. 6).

2.3. Sub-nanometer Structural Control

The lowest measured repeatability of the measurement corner cube surface scans indicates that there is a noise source inherent in the structure supporting the experiment, independent of the corner cube defects.

To measure the level of the structural noise, a length servo system that combines the detected motion of the measurement corner cube by the four outer heads in the 3-dimensional metrology system is used. The linear combination is selected to produce nearly full motion compansation in the direction monitored by the fifth, central gauge head. The fifth head is used to monitor the residual motion that is a direct combination of all the structural

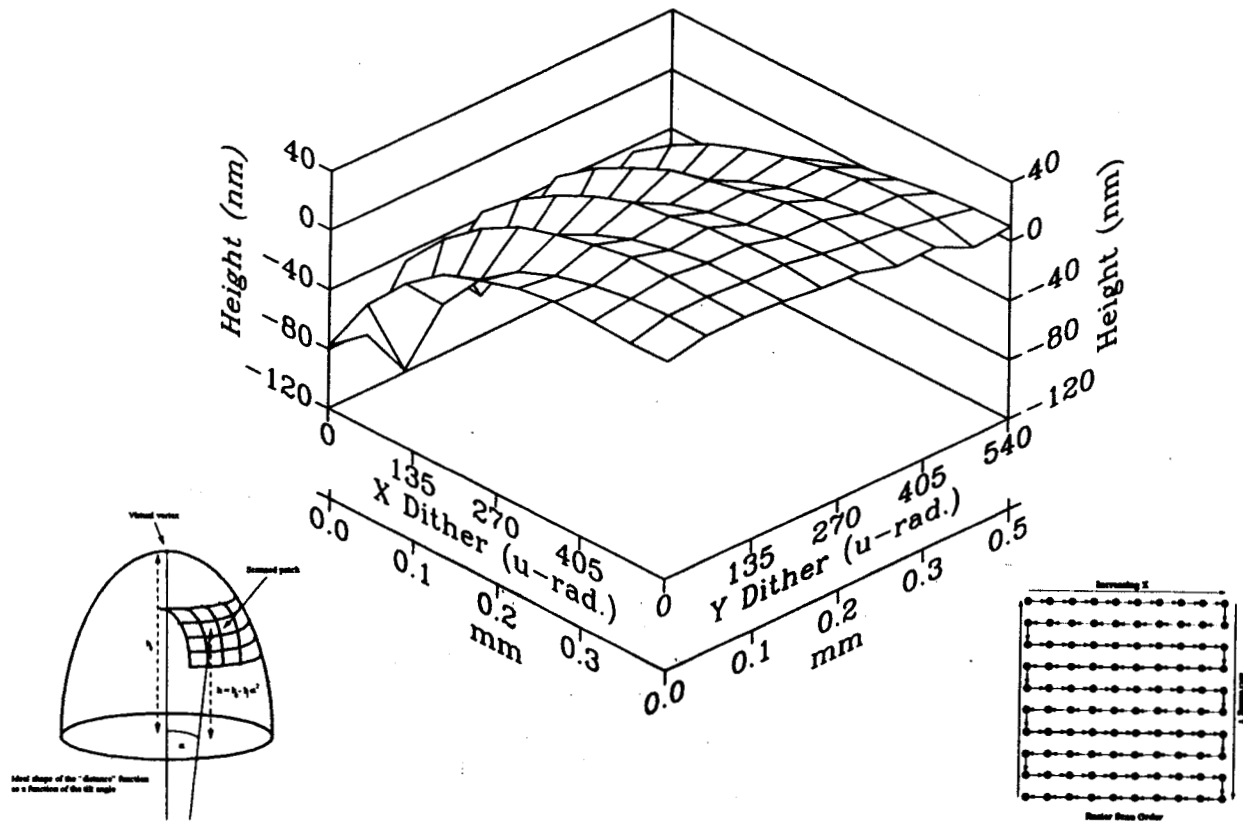Figure 7: The raster scan of the measurement corner cube in vacuum

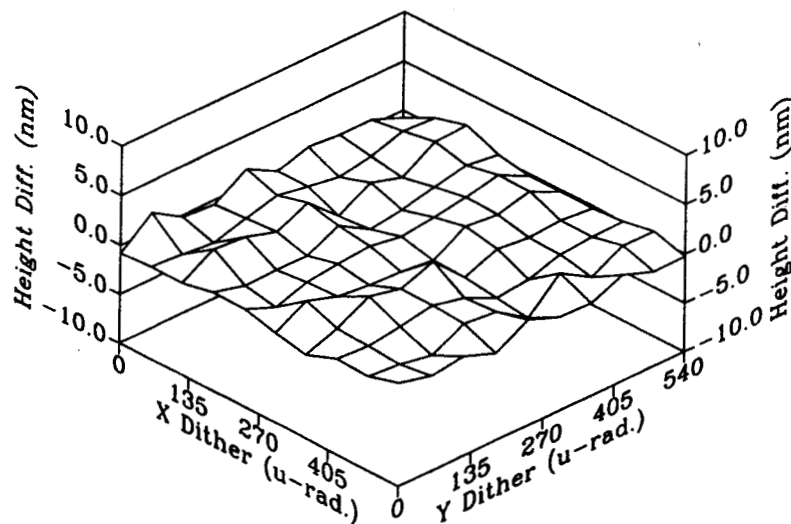Figure 8: The difference between two subsequent raster scans

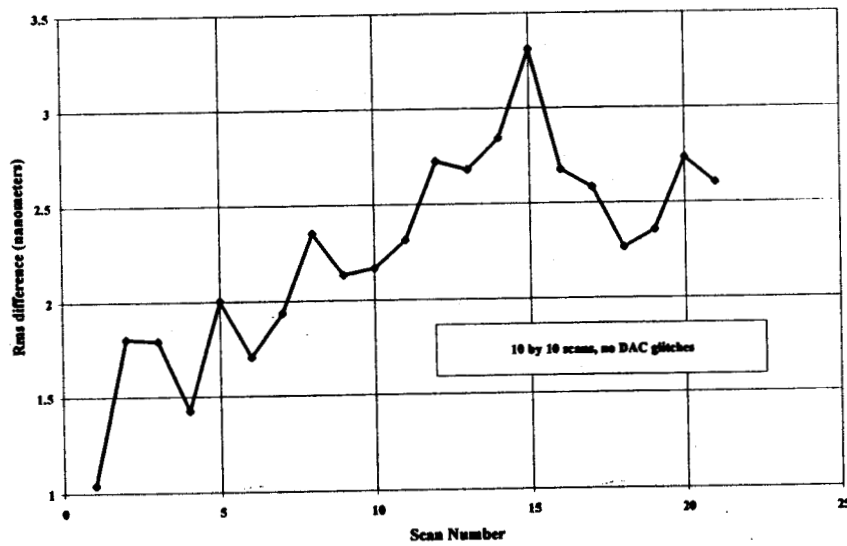Figure 9: The difference between the first surface scan and the following ones

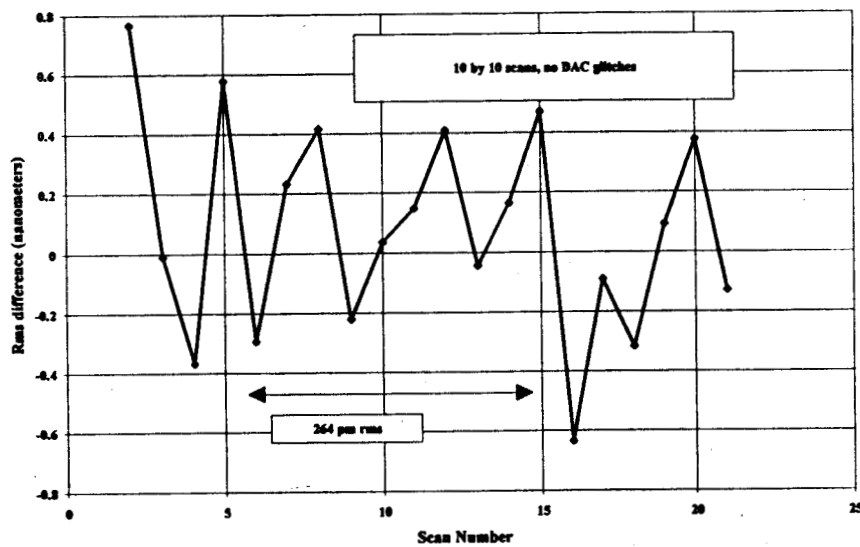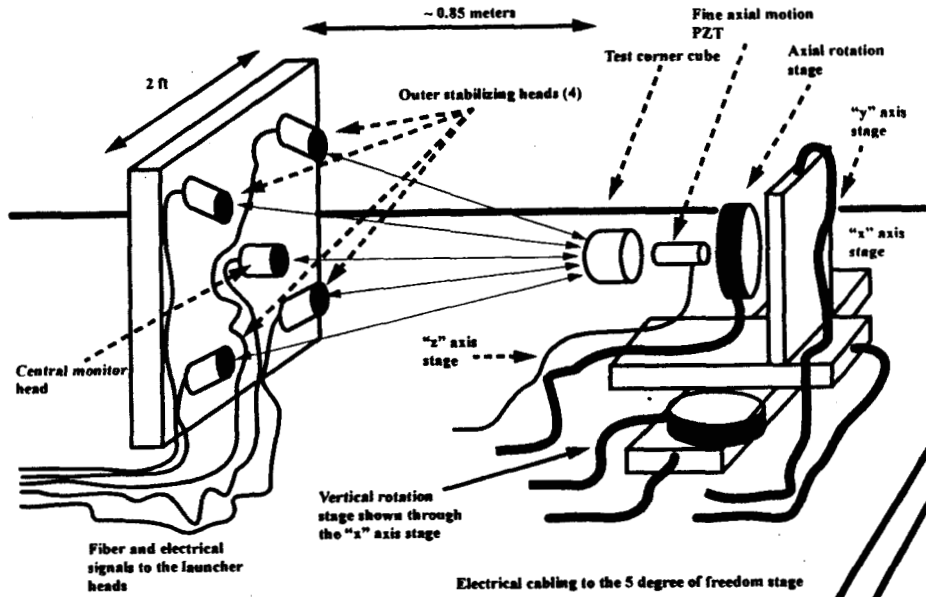Figure 10: The difference between subsequent surface scans

Figure 11: The 3-dimensional structure stabilized by light

~ 0.85 meters

2 ft

Outer stabilizing heads (4)

Fine axial motion PZT

Test corner cube

Axial rotation stage

"y" axis stage

"x" axis stage

Central monitor head

"z" axis stage

Vertical rotation stage shown through the "x" axis stage

Fiber and electrical signals to the launcher heads

Electrical cabling to the 5 degree of freedom stage

noise detected at the edges and at the center of the base plate. The experimental configuration is shown in Fig. 11.

Again, few technical problems had to be solved to make this system work with adequate sensitivity. Resonance of the flexure mount of the measurement corner cube limited the servo closed loop unity gain bandwidth to 666 Hz. This bandwidth was obtained by filtering the signal that was applied to the piezo-electric actuator that moved the measurement corner cube, in order not excite the mount mechanical resonance.

Other troubling noise sources were the vacuum pump induced vibrations, the room air handler induced vibrations and the tilting of the chamber with air-isolated legs due to changing ambient air pressure. These were avoided by shutting the vacuum pump off and by running the experiment automatically at night when the ambient conditions were more stable due to lack of activity by the lab personnel.

Fig. 12 shows the combined, closed-loop servo error signal generated by the four outer heads for 4000 seconds. This particular segment of the data was taken when the environmental disturbances were at a minimum. The root-mean-squared jitter in the residual error signal is about 0.6 pm rms with virtually no drift as expected.

Fig. 13 shows the length changes detected by the fifth, central head for the same duration when the servo system was running. During this particular segment, the drift detected by the central head is about 1 pm per second while the root-mean-squared jitter is 234 pm, closely matching the jitter in the z direction in the tracking runs as shown in Fig. 6 and the jitter in the repeatability of the surface scans of the measurement corner cube as shown in Fig. 10. This is the proof that all the jitter is caused by the structural noise.

Fig. 14 shows the time domain signal illustrated in Fig. 13 in the frequency domain. The vertical scale of the magnitude of the Fourier transform of the length signal is calibrated in such a way to read unit amplitude for a sinusoidal length change of unit amplitude with a frequency that falls on one of the bins of the digital Fourier transform. As illustrated, there are 1024 bins of frequency spanning a bandwidth of 8 Hz.

The head resonances cover a band between 6 and 8 Hz, and they are relatively insignificant. An alised pump vibration with original frequency just under 60 Hz appears as a sharp peak around 5.5 Hz. Almost all of the jitter is confined in a frequency band between 0 Hz and 2 Hz. At time the data were taken, there were not enough environmental sensors hooked up to the experiment to associate individual peaks in this band with specific disturbances. However, the some of the disturbances in this frequency band are identified and they are indicated in the illustration.

Figure 12: The combined, closed-loop servo error signal generated by the four outer heads
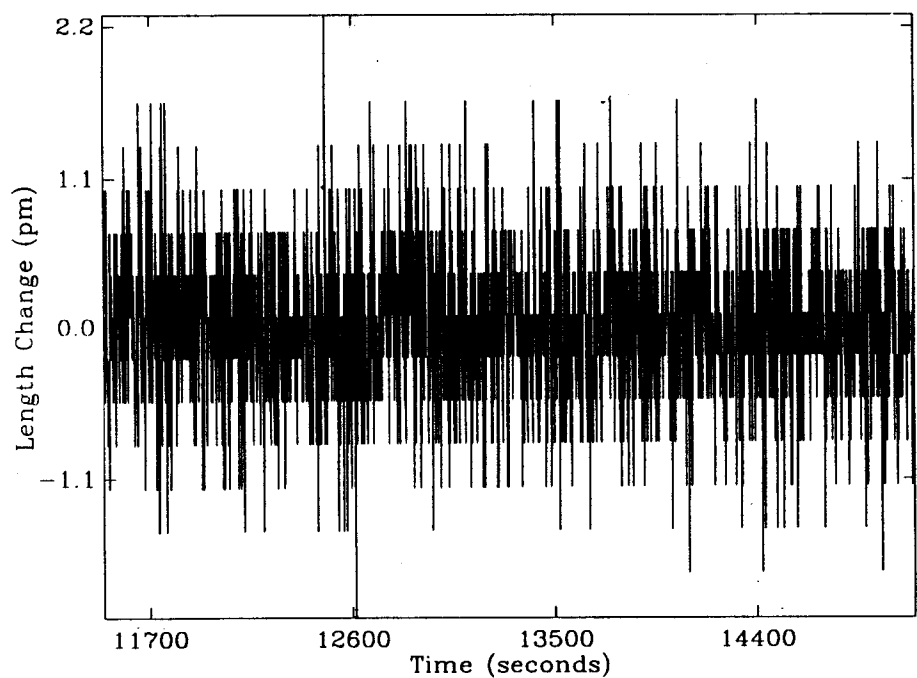

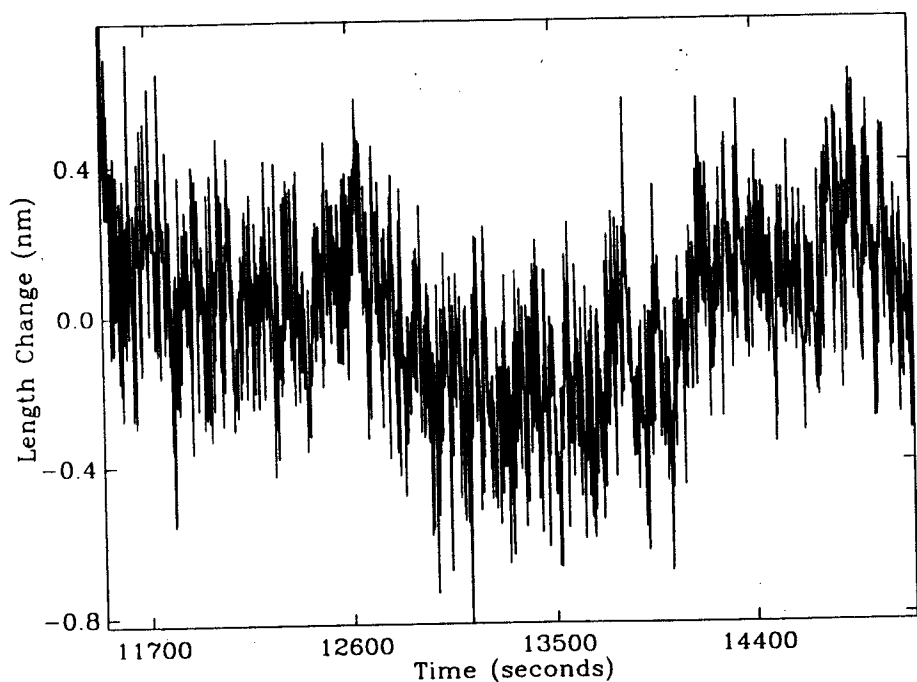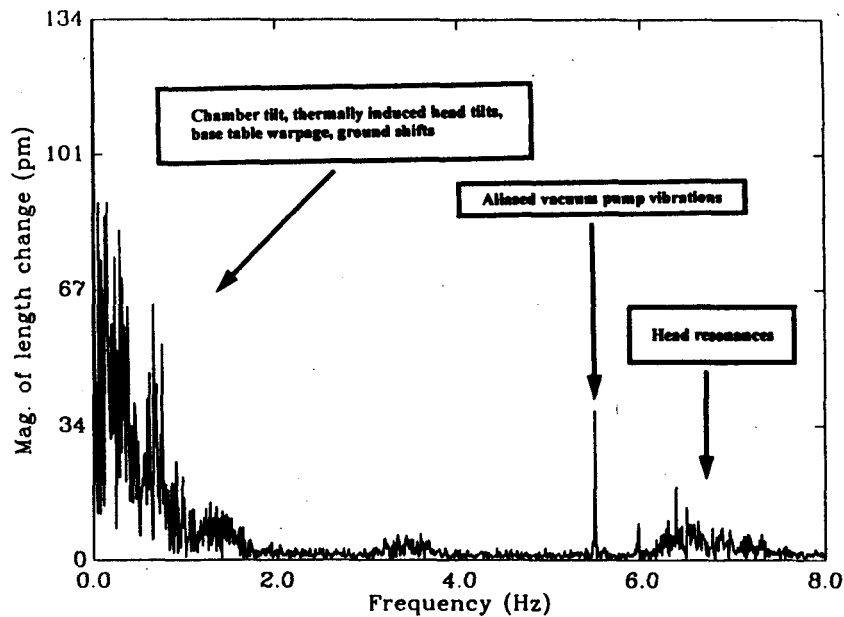Figure 13: The length changes detected by the fifth, central head

Figure 14: The detected length changes in the frequency domain

2.4. Improvements to the Experimental Setup

In order to eliminate or keep track of the environmental disturbances that could affect the 3-dimensional metrology experiment, following steps were taken.

A plastic shed was built around the entire chamber and its isolation system to prevent the erratic air flow produced by the air handlers from directly striking the thermally insulated chamber. The air flow mechanically shakes the chamber.

Ten temperature sensors were added to the experiment inside the chamber and outside the chamber to track all relevant temperature changes and pressure sensors are being added to track the inside and the outside pressure changes.

Head signal processing is modified to record the temperature stability of the analog signal processing circuitry itself as well as all DC and AC light levels. New 16 bit DACs are added to eliminate the glitching 8 bit DACs in addition to supplying more spatial resolution.

The gauge realtime software is extended to record 80 channels of environmental monitors simultaneously with the 10 laser gauge signals. The environmental monitors are recorded at a lower bandwidth of 1 Hz, while the laser gauge signals can be recorded at 16384 Hz or lower.

New mechanical hardware to re-locate the heads easily is being installed to test other experimental configurations and to optimize the location of the heads. New integrated optic fiber splitters are being installed to supply a more even distribution of light to the gauge heads.

2.5. What's Next?

Hardware modifications to the 3-dimensional metrology experiment will be completed first as this paper goes to print. After pumping down, new raster surface scans will be produced using the new 16 bit DACs.

In order to identify the cause of various noise sources as described in the previous sections, new four outer head servo experiments will be performed. The results of these experiments will be compared to new dithered tracking runs in vacuum to show that dithering eliminates any drift that looks like a head tilt, thereby reducing the detected jitter. At the same time, this procedure gives an indication of how much the changing head tilts are contributing

to the detected jitter. After the sources of the jitter noise are identified, the goal is to reduce it to a level below 100 pm rms.

Currently, the 3-dimensional metrology gauge heads are dithered mechanically. Due to the limited range and the response of this tilting system, the ultimate goal of reducing the jitter below 10 pm rms will be difficult. New light beam deflection systems, like the recently developed Meadowlark LCD beam deflector[12], will be installed to overcome the problems encountered with the present mechanical dithering system.

Implementation of absolute metrology for all of the 3-dimensional metrology gauge heads will eliminate all surveying guesses and related errors by constraining five more parameters in the surveying solution[5].

2.6. Simulations

2.6.1. The accuracy of the surveying solution

Exact data generators that simulated the motion of the measurement corner cube were written using the formulas given in my previous paper[5] to test the real data analysis programs. These were used in the verification of all my data analysis software. Recently, noise and drift generators were added to this software and the analysis software was extended so that it could solve for a global survey over many (as many as required) independent data sets.

The results of these simulations completely agree with the observed experimental behavior. If there is no noise and no drifts in the simulated data, the minimizer that extracts the surveying is able to find the actual, true survey if it is started within a few millimeters of it. However, even the slightest amount of white noise (1 nm rms) coupled with small drifts (100 pm per wavelength of OPD motion) is enough to push the minimizer away from the true solution by the observed amounts. The large deviation of the z location of the measurement corner cube from the crude survey value as reported in my previous paper[5] is readily traced to the inaccuracy of the crude survey. The location determined from data was a few cm off from the location that was crudely measured using the assembly pictures. This was done deliberately to test the system and the algorithms. After the experiment was functioning reliably, the vacuum chamber was opened and a more accurate mesurement was performed. The agreement between the crude survey and the survey extracted from the data is now uniformly the same on all coordinate axes: about a few mm ($\pm$ 4 mm maximum).

2.6.2. The effect of beam wavefront aberrations on the detected phase

In my previous paper[5], the detected phase for a heterodyne interferometer with aberrated and non-gaussian wavefronts was defined. Given "reasonable" wavefronts A and B with finite extent, the interference at the photodetector of the heterodyne gauge is given by (Eq. (1) of the previous paper):

$$Interference = \left\langle \left| \alpha A + \beta B \right|^2 \right\rangle = \left\langle (\alpha A + \beta B) \ (\alpha A + \beta B)^* \right\rangle, \tag{1}$$

where $<>$ denotes time average and spatial integration over the intersection of the bounded supports of the entire wavefronts A and B, and α, β are constants that are determined by the details of the detection mechanism. In a heterodyne interferometer, α is nearly equal to β in magnitude. These constants are determined by the quality and the angular setting of the detection polarizer.

Let $I_a = < |A|^2 >$ and $I_b = < |B|^2 >$ be the total intensities contained in the wavefronts A and B. The phase of the complex number $\gamma = < BA^* > / < |A|^2 >$ is the phase detected by the interferometer relative to the phase of A. Let $\delta = \alpha\beta^*\gamma^* + \alpha^*\beta\gamma$ where α, β and γ are as defined above, $*$ denotes the complex conjugation and δ is a real number.

The interference given by Eq.(1) can now be written as:

$$Interference = |\alpha|^2 \left\langle |A|^2 \right\rangle + |\beta|^2 \left\langle |B|^2 \right\rangle + \delta \left\langle |A|^2 \right\rangle. \tag{2}$$

Figure 15: The intensities of the two interfering spots
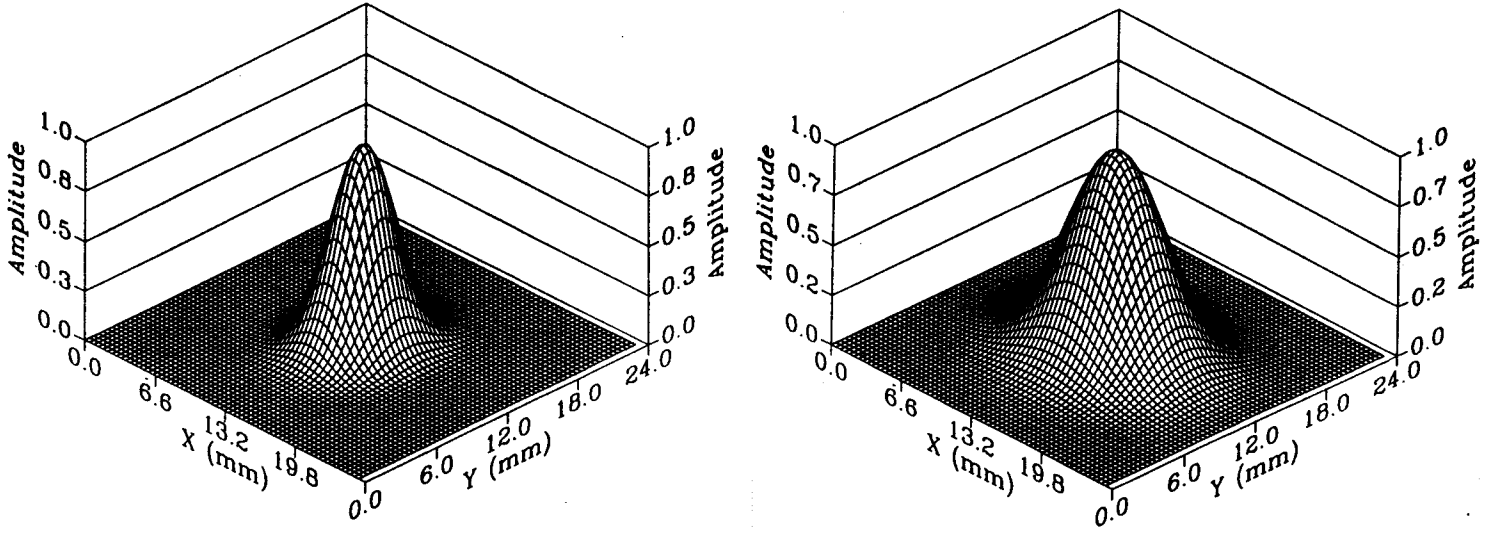
I define the fringe contrast c as:

$$c = \frac{|\delta|}{\left[|\alpha|^2 + |\beta|^2 I_b/I_a\right]}.$$

(3)

Note that if $\alpha = \beta$ and $A = B$, the $c = 1$. If $\gamma = 0$ (no interference), then $c = 0$. Note also that c can reach the value 1 for a particular set of wavefronts A and B, for particular values of α and β. This is the reason why the fringe contrast is not a good quality-indicator for the heterodyne laser gauge unless the wavefronts A and B are close to each other and α, β are nearly equal in magnitude and phase.

A spot simulator is written that can generate spots with expected aberrations. The generated spots are sheared with respect to each other to simulate a misaligning heterodyne gauge head. The detected phase and the fringe contrast as given by γ and Eq.(3) as well as the spot intensity and phase patterns are shown in the following figures. The spots were sheared along a path that made equal angles with the x and the y axes in the spot plane.

For a variety of expected spots, the detected phase can change by 10 pm to 100 pm for a total shear of 500 μm on the detector plane while the fringe contrast only changes by a few percent. Comparison with the 3-dimensional metrology spot shapes indicate that this may be the next noise source to tackle, to reduce the detected tracking jitter below 100 pm rms.

2.7. The Ball Fiducial

One of the classic designs for a very wide angle retroreflector is the hemi-spherical cat's eye retroreflector as schematically shown in Fig. 19. The laser beam enters through smaller hemisphere, and is focused on the coated back surface that retroreflects it back. The field of view of this retroreflector is nearly 2π steradians.

Let R_a and R_b be the radii of the hemi-spherical pieces as shown. Given a particular glass type with an index of refraction n, the relationship between R_a to R_b is given by $R_b = [1/(n-1)]R_a$. The main problem with a perfect hemi-spherical retroreflector is amount of spherical aberration imposed on the reflected beam. There are many improvements on this basic design that give less spherical aberration, including a layered, hemi-spherical cat's eye retroreflector[13].

The main problem in manufacturing a perfect hemi-spherical cat's eye is accurate cutting and re-gluing of the
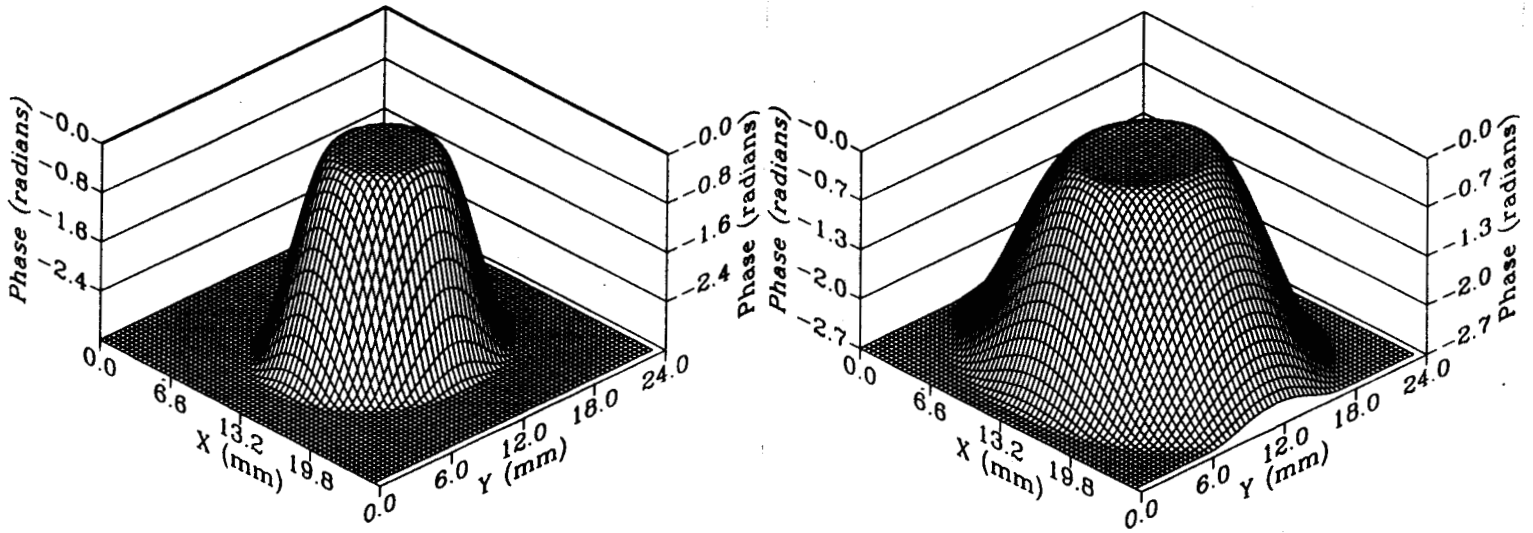
Figure 16: The phases of the two interfering spots

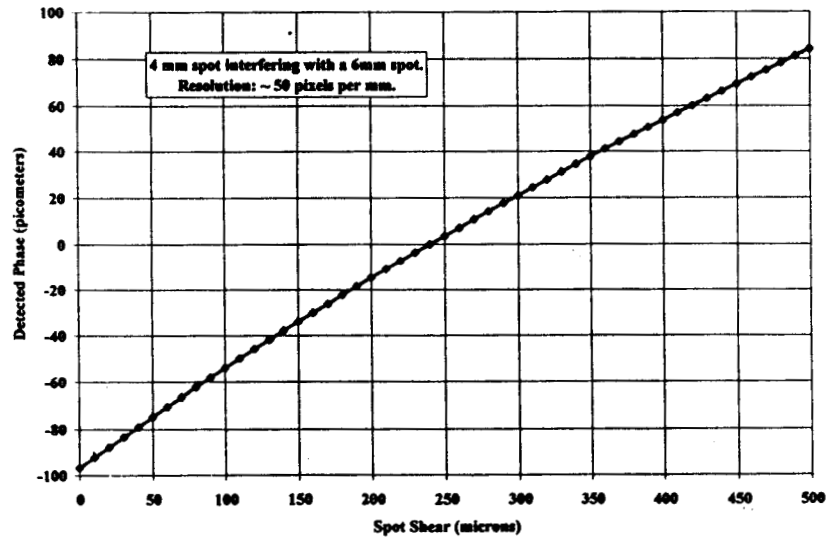Figure 17: The change in detected phase due to shear

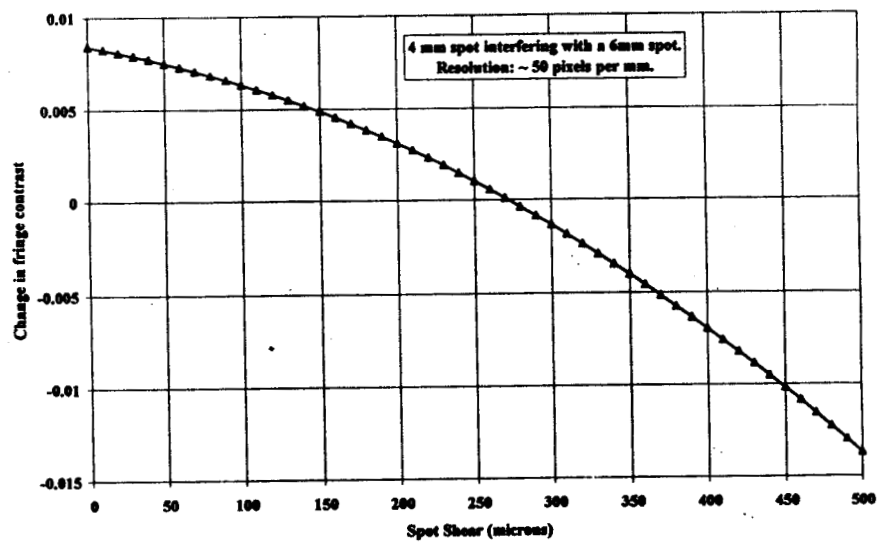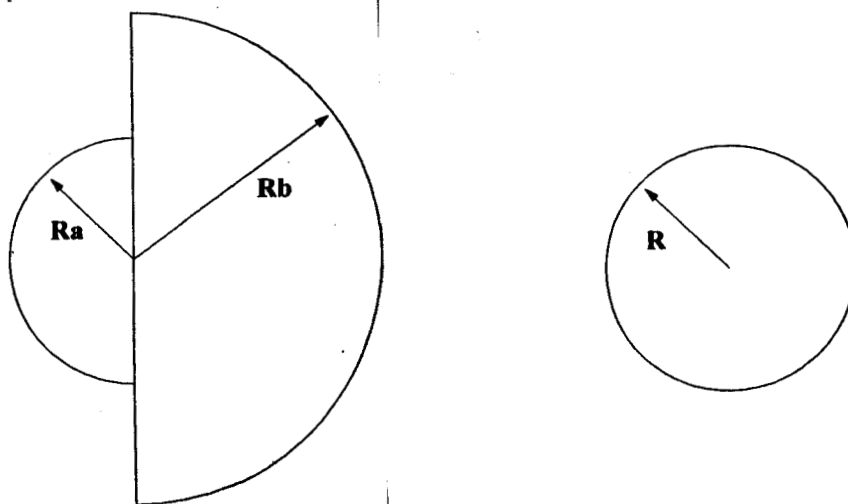Figure 18: The change in fringe contrast due to shear

Figure 19: The hemi-spherical and the fully spherical cat's eye retroreflectors

hemi-spherical halves. It is very difficult to locate the centers of the halves within a micron of each other. This puts a very tight and hard to meet constraint on the accuracy of the absolute metrology gauges for spatial interferometry.

All of the manufacturing problems can be solved by choosing a glass with an index of refraction of 2 at the desired wavelength. This makes $R_a = R_b = R$ resulting in a perfect sphere (Fig. 19). Using standard polishing techniques, a 40 mm ball can be polished to a surface accuracy of $\lambda/20$ at 633 nm. This results in a retroreflector with a common corner co-location error of around 40 nm and with a returned-beam spherical aberration around $\lambda/4$ for an incident, 5 mm diameter laser beam. The only difficulty is finding a glass with the desired qualities.

The Schott glass LaSF-35[14] satisfies almost all of these constraints: Its index of refraction at 780 nm is 2.000. Its dn/dT, the change in index of refraction as a function of temperature, is one of the lowest among common glasses, 1×10^{-6} per degree K. Its coefficient of thermal expansion is 8.5×10^{-6} per degree K. To maintain a fiducial end point stability of 40 pm with a 40 mm LaSF-35 ball requires sub-millidegree temperature control which is well within the current technology[3][8]. The field of view of the ball fiducial with half of its surface coated with a highly reflective coating is nearly 2π steradians. This field-of-view can be doubled by using two different frequency lasers and narrow band, wavelength selective coatings that either cover the whole ball or are applied to small patches around its surface. In very high input intensity applications, bare ball can be used with its full field of view, using the collimated reflections from the glass-to-air surface.

This particular glass is very hard to manufacture in large, uniform and homogeneous chunks due to its low viscosity and fast heat conduction when it is molten. It is made for manufacturing GRIN lenses that tend to have small diameters around a few millimeters. Its manufacturer does not exclude the possibility that they might be able to make large enough pieces to polish a 40 mm ball, but they also indicate that this requires further research on their part.

The only remaining problem is the path length changes induced by the inhomogeneities in the glass as the gauge beams move through the fiducial. Since in a metrology system, the path of the moving the beams are well known in advance, this particular source of systematic error can be calibrated out easily.

3. SUMMARY

The tracking jitter in the 3-dimensional metrology experiment is traced to structural noise induced by environmental changes. The current jitter is about 250 pm rms in the z direction, and about 600 pm rms in the x and y directions, for motions of the order of 10 wavelengths of OPD at a wavelength of 1319 nm, in vacuum at a pressure level of about 15 milliTorr.

The solution for surveying is shown to be very sensitive to Gaussian white noise and drift in the gauge data. For a noise level of 1 nm rms and for drifts of the order of 100 pm per wavelength of OPD of motion, the simulations match the actual experimental results.

The simulated aberrations in the gauge beam wavefronts are shown to cause systematic drifts and noise in the detected phase. However, the noise is not large enough to explain the currently observed jitter.

A wide angle retroreflector fiducial design that results in a very low common corner co-location error of few tens of nanometers, as opposed to few microns co-location error of the current open face retroreflector derivatives, is presented. The design is shown to be feasible using current commercial technology.

4. ACKNOWLEDGEMENTS

5. REFERENCES

1. Y. Gürsel, Laser metrology gauges for OSI, *in Proceedings of SPIE conference on Spaceborne Interferometry*, Vol. 1947, p. 188-197, 1993.

2. Y. Gürsel, Metrology for spatial interferometry, *in Proceedings of SPIE conference on Amplitude and Intensity Spatial Interferometry*, Vol. 2200, p. 27-34, 1994.

3. Y. Gürsel, Metrology for spatial interferometry II, *in Proceedings of SPIE conference on Spaceborne Interferometry II*, Vol. 2477, p. 240-258, 1995.

4. Y. Gürsel, Metrology for spatial interferometry III, *in Proceedings of SPIE conference on Space Telescopes and Instruments IV*, Vol. 2807, p. 148-161, 1996.

5. Y. Gürsel, Metrology for spatial interferometry IV, *in Proceedings of SPIE conference on Small Spacecraft, Space Environments, and Instrumentation Technologies*, Vol. 3116, p. 12-26, 1997.

6. Robert D. Reasenberg, Robert W. Babcock, Marc A. Murison, M. Charles Noecker, James D. Phillips, Bonny L. Schumaker, James S. Ulvestad, William McKinley and Robert J. Zelinksy, POINTS: high astrometric capacity at modest cost *via* focused design, *in Proceedings of SPIE conference on Space Telescopes and Instruments IV*, Vol. 2807, p. 32-50, 1996.

7. E. Schmidtlin, S. B. Shaklan, A. E. Carlson, Novel wide field-of-view laser retroreflectors for space interferometry mission, *in Proceedings of SPIE conference on Astronomical Telescopes and Instrumentation, Astronomical Interferometry, poster session*, this volume, in press, 1998.

8. LABORATORY DIFFERENTIAL TEMPERATURE SOURCE and MODEL LT 100 THERMOMETER, Electro Optical Industries, Inc., 859 Ward Drive, Santa Barbara, CA., U.S.A., 1994.

9. Michael M. Shao and Donna M. Wolff, Orbiting stellar interferometer, *in Proceedings of SPIE conference on Spaceborne Interferometry II*, Vol. 2477, p. 228-239, 1995.

10. R. L. Baron, SIM vs. SOS: a space interferometry trade study, *in Proceedings of SPIE conference on Astronomical Telescopes and Instrumentation, Astronomical Interferometry*, this volume, in press, 1998.

11. J. W. Yu, J. Marr, R. L. Stoller, P. Kahn, SIM Interferometer design, *in Proceedings of SPIE conference on Astronomical Telescopes and Instrumentation, Astronomical Interferometry*, this volume, in press, 1998.

12. Michael H. Anderson, A Liquid Crystal Beam Steerer for Precision Interferometric Gauges, *NASA SBIR 96-1 Proposal # 10-01 4068 and following grant*, Meadowlark Optics, Inc., and National Aeronautics and Space Administration (NASA), 1996.

13. Walter Zurcher, Raimund Loser, Stephen A. Kyle, Improved reflector for interferometric tracking in three dimensions, Optical Engineering, Volume 34(9), p. 2740-2743, 1995.

14. SCHOTT OPTICAL GLASS, LaSF-35 1022291, Catalog Nr. 10,000, SCHOTT Glass Technologies, Inc., Duryea, PA., U. S. A., 9/1992.